# Detection and Quantification of Nonlabeled Polystyrene Nanoparticles Using a Fluorescent Molecular Rotor

Angélique Moraz and Florian Breider*

Cite This: https://doi.org/10.1021/acs.analchem.1c02055

Read Online

ACCESS | Metrics & More | Article Recommendations | SI Supporting Information

**ABSTRACT:** Plastic pollution has reached alarming levels in recent years. While macro- and microplastic pollution are attested and studied since the 1970s, much less is known about the associated nanoscopic fragments. Due to their ability to cross biological barriers and their extended surface area-to-volume ratio, nanoplastics (NPs) are currently considered as one of the major threats for aquatic and terrestrial environments. Therefore, analytical tools are urgently needed to detect and quantify NPs. In this study, a method exploiting the dependence of the fluorescence quantum yield of a probe, namely, 9-(2,2-dicyanovinyl)julolidine (DCVJ), toward its microenvironment



was assessed to detect and quantify polystyrene nanoplastics (PSNs). In the presence of PSNs and after excitation at 450 nm, the single-emission band fluorescent molecular rotor (FMR) emission spectrum displays a second peak at 620 nm, which increases with the concentration of PSNs. In pure water, a limit of detection and quantification range of $475-563$ $\mu g \cdot L^{-1}$ and $1.582-1.875$ $mg \cdot L^{-1}$, respectively, were obtained for 49 nm diameter polystyrene beads (PSB49). The results associated with 100 nm diameter PSNs amount to 518 $\mu g \cdot L^{-1}$ and 1.725 $mg \cdot L^{-1}$. The robustness of the method toward different parameters, the complexity of the matrix, and the PSN characteristics was also assessed. Finally, the method was applied on biological samples. While PSB49 quantification was achieved using radish sprouts at concentrations up to 200 $mg \cdot L^{-1}$, it was more challenging when handling mussel tissues. This work presents the feasibility to quantify PSNs using DCVJ fluorescence. It paves the way to new perspectives in the challenging field of NPs.
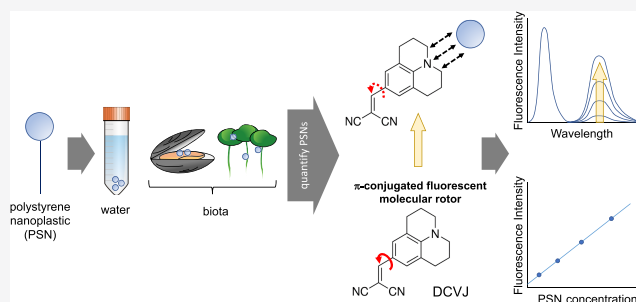
## INTRODUCTION

Annual plastic production has dramatically increased in the past few decades to reach almost 370 million tons worldwide in 2019.[1] The low cost, versatility, lightness, and resistance of plastics explain the exponential growth of their manufacturing in the 1950s. However, plastic waste management soon became a real issue. All around the world, plastic waste accumulates over the years and represents one of the major threats for aquatic and terrestrial environments.

Plastic littering in water bodies was first scientifically reported in the 1970s.[2] The mass of plastic ending up in oceans yearly is estimated at 8 million tons.[3] Small plastic particles arising from the degradation and flow of consumer goods such as shoe soles, tires, road painting, cosmetics, or synthetic fabrics carried by domestic sewage are colonizing wild environments invisibly but equally, or more critically, compared to items visible with the naked eyes.[4-6] The particles are nowadays ubiquitous in the marine environment, going from low concentration to localized "hotspots".[7] Freshwater plastic pollution, attested in rivers and lakes, is also a real environmental concern in non-coastal countries.[8]

Having regular or irregular shapes, the most visible and easily cleaned up debris is macroplastics (>25 mm). Plastic items with a size between 5 and 25 mm are often referred to as

mesoplastics.[9] Beyond this size limit, micro- and nanoplastics have been described. Microplastics (MPs) are defined as particles smaller than 5 mm. However, there is no universal consensus regarding the size from which they fall into the category of nanoplastics (NPs). Following Gigault et al.'s definition, NPs are not only characterized by their size, "ranging from 1 to 1000 nm", but also by their colloidal behavior.[10]

MPs and NPs can be found in the environment as primary or secondary particles. While primary particles were intentionally manufactured as such for a specific consumer good, secondary particles result from the degradation and fragmentation of plastic waste due to environmental stressors such as mechanical abrasion, ultraviolet photodegradation, biological metabolism, and chemical alteration.[11]

A

Depending on their size, plastic particles can cause not only physical but also chemical harm to local wildlife due to the leaching of contaminants from the plastic particles.[12] Ecotoxicological effects are increasingly assessed, and NPs are presumably more harmful than MPs. They can cross more biological and terrestrial barriers. By entering all trophic levels and affecting gene expression, cell function, cell morphology, and the hormone system, NPs can play the role of endocrine disruptors and have dramatic consequences on biodiversity.[13−19] The research in the field is relatively recent, and a lot of work is still necessary to fully elucidate the fate and impact of NPs in the environment and biological tissues.[20]

While promising detection techniques are emerging, it is urgent to improve, optimize, and standardize analytical protocols as well as validate new ways to quantify NPs in various matrices. Due to their small size, all steps of the analytical process to study NPs in an environmental sample, including extraction, sorting, detection, and quantification, are challenging. MP research began earlier than the study of NPs, but the related findings cannot be extrapolated because their physical and chemical properties differ. Their size confers them a colloidal behavior that hinders the use of some of the methods developed to analyze MPs.

Exploiting the properties of light when interacting with matter, techniques like dynamic light scattering (DLS), multiangle laser scattering (MALS), and nanoparticle tracking analysis (NTA) can estimate the size of NPs. Electron microscopy goes a step further by providing additional information on the shape and morphology. However, quantification is difficult and the sophistication of the apparatus can make it expensive, difficult to handle, and time-consuming.[21]

Raman microspectroscopy (RM) and Fourier-transform infrared spectroscopy (FT-IR) are two complementary spectroscopic techniques proposed to investigate the chemical nature of NPs.[22] X-ray spectrometry, such as energy-dispersive (EDS), provides additional information about the elemental composition of the sample. X-ray photoelectron spectroscopy (XPS) can be exploited to characterize the sample surface by analyzing the binding energy of the emitted photoelectrons. However, like FT-IR, XPS cannot be used for single-particle analysis but rather for collection measurements.

In addition, a pyrolysis variant of the commonly known gas chromatography−mass spectrometry (Py-GC−MS) has been reported for NP chemical identification.[23] However, the method requires a preconcentration step and the sensitivity still needs to be improved to match the predicted NP environmental concentrations. In addition, Py-GC−MS suffers from poor interlaboratory reproducibility.[24]

Inductively coupled plasma mass spectrometry (ICP-MS) operating in single-particle mode has also been proposed. Although 1 and 2.5 $\mu$m PS particles were successfully detected, the applicability size range is at present higher than the NP diameter, except if the particles are labeled with metal, making the methods yet not applicable to environmental samples.[25,26]

Exploiting metal, radioactive, or fluorescent labels, NPs can be detected and quantified using microscopy, autoradiography, or ICP-MS.[27−30] However, it can only be used for ecotoxicological studies or as an internal standard to assess a protocol such as the retention of NPs by wastewater treatment plants. In addition, all other steps of the method must be properly chosen to minimize undesired interference with the label.[22] In brief, there is currently no scalable analytical method for determining the NP concentration in environmental samples.

The aims of the present study were (i) to investigate and further develop an innovative method based on the initial work of Bisso et al. and Gagné,[31,32] exploiting the modulation of a fluorescent molecular rotor (FMR) emission, namely, 9-(2,2-dicyanovinyl)julolidine (DCVJ; Figure S1), to detect and quantify polystyrene nanoplastics (PSNs) in biological samples and (ii) to assess the influence of temperature, viscosity, NP characteristics, natural organic matter (NOM), and the matrix on the sensitivity of the method. An FMR is a fluorescent organic compound consisting of an electron donor unit bound to an electron acceptor by an unsaturated electron-rich linker.[33] Upon excitation, it accesses either a planar or twisted excited state, the distribution depending on the microenvironment. Then, depending on the excited state and the energy gap in the twisted one, the relaxation is either radiative or non-radiative. Exploiting the sensitivity of their fluorescence quantum yield toward viscosity, some FMRs have already been used as microviscosity sensors.[34,35] Their torsional motion is sterically hindered by the viscosity, and the non-radiative deexcitation rate decreases. In turn, the fluorescent pathway is favored, and its signal intensity increases. Recent studies suggest that interactions or binding with surrounding particles or macromolecules, such as NPs, lead to the same phenomenon since the molecule rotation is similarly impeded.[32,36] However, Gagné's report on the DCVJ method was found to be cursory. It is thus valuable to reinvestigate thoroughly the NP quantification method.

## ■ MATERIALS AND METHODS

**Chemicals and Materials.** All purchased PSNs were presented as aqueous suspension. PSNs with diameters of 100 and 300 nm (LB1 and LB3, 10% solid) were acquired from Sigma-Aldrich (St. Louis, MO, USA). Nonfunctionalized (PSB49, Polybead Microspheres, 2.6% solid, catalog number: 08691-10) and carboxyl-coated (PSB49coo, Polybead Microspheres, 2.7% solids, catalog number: 15913-10) PSNs with a diameter of 49 nm were obtained from Polysciences (Warrington, PA, USA). Both radish seeds (*Raphanus sativus* L.) and mussels (*Mytilus edulis*, farmed in Holland) were purchased at Migros (Switzerland). 9-(2,2-dicyanovinyl)-julolidine (DCVJ), sodium chloride (NaCl), 4-(2-hydroxyethyl)piperazine-1-ethanesulfonic acid, *N*-(2-hydroxyethyl)piperazine-*N*′-(2-ethanesulfonic acid) (HEPES), (ethylenedinitrilo)tetraacetic acid (EDTA), DL-1,4-dithiothreitol (DTT), and potassium hydroxide (KOH) were all obtained from Sigma-Aldrich (Switzerland). Sodium hydroxide (NaOH) and glycerol were purchased from Merck Millipore (Switzerland). Natural organic matter (NOM) from the Upper Mississippi River (RO Isolation) was obtained from the International Humic Substances Society (IHSS, USA). All solvents were analytical grade from Sigma-Aldrich (Switzerland). Syringe filters (CHROMAFIL Xtra H-PTFE, 25 mm, 0.45 $\mu$m) were obtained from Macherey Nagel (Germany). Unless specified otherwise, H$_2$O mentions in this work refer to Milli-Q water obtained from a reference water purification system from Merck Millipore. It was used to prepare the PSN solutions unless another solvent is mentioned.

**Instrumentation and Measurement Protocol.** A Biotek Synergy MX microplate reader in fluorescence mode was used to monitor the DCVJ's emission signal intensity spiked with the samples in 96-well plates (Microfluor 1 black plate, flat

bottom wells) from VWR (Switzerland). The measurement protocol settings were defined using the Gen5 1.11 software. The samples were pipetted and gently mixed with the pipette to homogenize the PSN and DCVJ solutions (total volume of 250 $\mu$L per well). The microplate was shaken inside the chamber of the instrument, and a delay was then applied before scanning the first well of the plate to ensure that the samples were at equilibrium. Four replicates were measured for each sample and blank. See the Supporting Information for more details.

**Preliminary Measurements.** See the Supporting Information for details concerning the absorption, fluorescence, and dynamic light scattering measurements.

**Investigation of Existing Findings.** The method proposed by Gagné was assessed first in pure water (see the Supporting Information for details).[32]

**DCVJ Fluorescence Analysis.** See the Supporting Information for details about the effect of the solvent, pH, and light exposure on the DCVJ fluorescence spectrum.

**Optimization of the Analytical Protocol.** All parameters and tests are described in Tables S1 and S2. Along with the variation of the instrument settings, the proportion of MeOH over $H_2O$ in the microplate wells as well as the size and concentration of the latter was modified. According to the literature, the smaller the particles are, the more sensitive the method is.[32,37] It was thus decided to focus on the smallest PSNs available at the time of the experiment. Further tests were conducted (Supporting Information, Sections S2.5−S2.10) to study the influence of the temperature, the magnitude of the PSN specific surface area, the nature of the PSN chemical surface, the matrix, and its viscosity on the robustness of the method, which is evaluated by the quality of the calibration.

**PSN Quantification in Vegetal Samples.** The optimized setup was selected (Listing S1). Fifty radish seeds were grown in a glass crystallizer on cotton wool humidified with tap water. A constant temperature of 25 °C, suitable humidity conditions, and continuous light exposure were ensured. One week later, the ≈3 cm long sprouts were cut at the stem base (while avoiding collecting cotton wool) and dried for 2 h at 60 °C. The dry sprouts were finely crushed with a mortar and pestle. The preparation of the standards and samples and the details of the tests are given in the Supporting Information (Section S3.1).

**PSN Quantification in Animal Samples.** Fresh mussels were defrosted and cooked to open their shell. After removing the shell, they were ground with a mixer. The resulting paste was diluted at 16% (w/v) in 50 mM NaCl including 10 mM Hepes-NaOH (pH 7.4), 1 mM EDTA, and 1 mM DTT (D1 mix, from Gagné[32]). The solution was centrifuged for 15 min at 3000 rpm. The supernatant (Sdiluted16%) was collected. It was mixed with either $H_2O$ or DCVJ (40 $\mu$M, MeOH) in the microplate to perform test MU-1. For tests MU-2 and MU-3, fresh mussels were defrosted, cooked, and dissected for the stomach (Figure S24). The stomachs from some 20 individuals were pooled and freeze-dried for one night. The fine mussel stomach powder (MSP) obtained after crushing with a pestle was diluted at 20 mg·$L^{-1}$ in $H_2O$ to prepare the mussel matrix. While the matrix was filtered (0.45 $\mu$m PTFE) before being spiked with PSB49 for the test MU-2, no filtration was performed for MU-3. An additional digestion step was included in tests MU-4 and MU-5 using the D1 mix or KOH 10%, respectively. The matrix (10 mL, 5 g·$L^{-1}$ MSP in

either D1 mix or KOH 10%) and two 10 mL samples (5 g·$L^{-1}$ MSP in either D1 mix or KOH 10% spiked with PSB49 at 10 mg·$L^{-1}$, respectively, 20 mg·$L^{-1}$) were prepared in glass tubes and immersed in a water bath (90 °C). After 3 h, the tubes were centrifuged (3000 rpm, 15 min) and the supernatant was collected. The same procedure as for MU-4 and MU-5 was followed for MU-6 and MU-7, except that the samples were spiked with 5 and 15 mg·$L^{-1}$ PSB49 and standards were also prepared by spiking PSB49 (0, 0.9, 1.8, 3.6, 7.2, and 14.4 mg·$L^{-1}$) in the matrix supernatant after centrifugation. The digestion duration (D1 mix or KOH 10%, heating plate at 90 °C) was extended to 24 h. Table S12 summarizes the analyses performed with the mussel's tissues.

## ■ RESULTS AND DISCUSSION

In all figures displaying the results, the written concentrations are the ones in the microplate wells. The data points correspond to the arithmetic mean computed over the quadruplicates. The blank refers to a sample without PSNs but with the same DCVJ concentration and same matrix as samples containing PSNs.

**Optimization of the Analytical Protocol.** Even if the temperature can be selected on the Gen5 software, it was generally not possible to stabilize it for a long time. The temperature often varied between the start and the end of the measurement (variation between 0 and 1.1 °C). The results presented in Gagné's report could not be reproduced (see the note in the Supporting Information, Section S2.2).[32] The major issues were the appearance of the blank as the most intense signal and the absence of the 620 nm peak used by Gagné for NP quantification. Although the DCVJ emission spectrum two-peak pattern resembles the one in Gagné's paper and the peak maxima are situated at the same wavelengths, namely, 510 and 570 nm, compared to Gavvala et al.'s study,[38] it was impossible to quantify PSNs. The curves associated with the different PSN concentrations were indistinguishable (Figure S2). Therefore, different tests were performed to obtain a workable calibration to quantify PSNs (Table S2). The most beneficial protocol optimization was to change the proportion of MeOH over $H_2O$ in the microplate wells. Instead of using 200 $\mu$L of 10 $\mu$M DCVJ, diluted in $H_2O$ from a 1 mM DCVJ in MeOH, and 50 $\mu$L of the analyte, it was decided to add 50 $\mu$L of DCVJ solubilized at 40 $\mu$M in pure MeOH to 200 $\mu$L of the analyte. The spectral features changed, and there was no more peak at 570 nm but rather the one at 620 nm. The underlying mechanism of its significant growth with the PSN concentration is believed to be a hydrophobic interaction between DCVJ and the surface of the beads, most probably the $\pi-\pi$ interactions between their aromatic rings. This remains to be clarified, but it is likely that the formation of emissive dimeric or oligomeric species contributes also to this 620 nm peak. PSNs could play the role of a nucleation substrate for DCVJ aggregation. Compared with Gavvala et al.'s paper, the excimer peak seems red-shifted from 570 to 620 nm due to the change of the DCVJ solvent, more precisely, the proportion of MeOH over $H_2O$. Additional tests led to important findings. At equal mass concentration, the larger the PSN, the more challenging the quantification. The spectra associated with the different LB3 concentrations are close to each other compared to the well-defined spectra in the presence of LB1 concentrations ranging from 0.9 to 14.4 mg·$L^{-1}$ (Figures S6 and S7). The curves associated with the 4−64 $\mu$g·$L^{-1}$ LB1 concentration are relatively stacked together
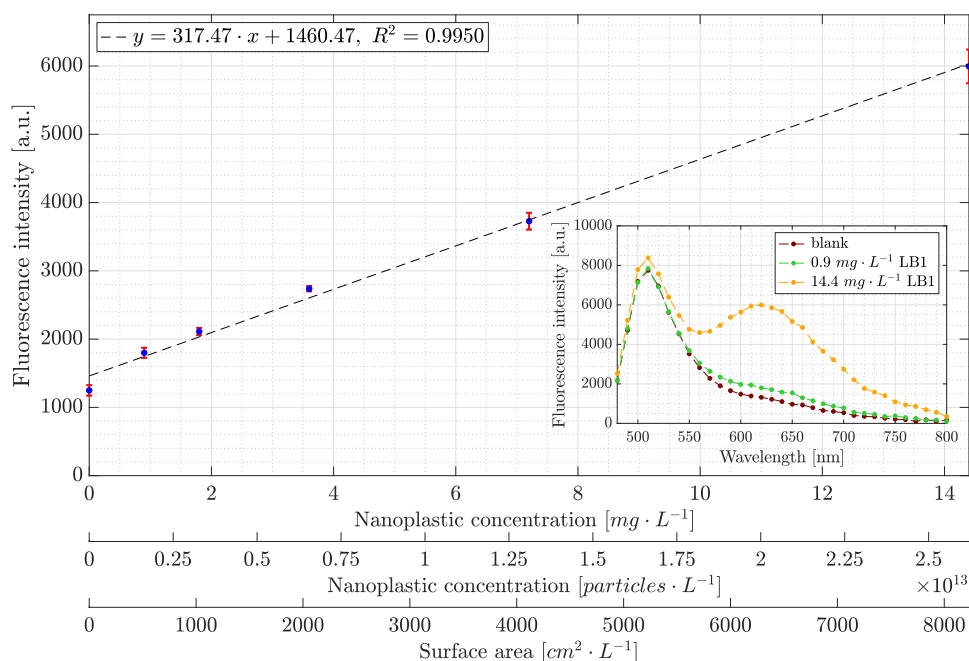
**Figure 1.** DCVJ fluorescence intensity as a function of the LB1 concentration in terms of mass (0, 0.9, 1.8, 3.6, 7.2, and 14.4 mg·L$^{-1}$), number of particles (0, 1.64 × 10$^{12}$, 3.27 × 10$^{12}$, 6.55 × 10$^{12}$, 1.31 × 10$^{13}$, and 2.62 × 10$^{13}$ particles·L$^{-1}$), and surface area (0, 514, 1029, 2057, 4114, and 8229 cm$^2$·L$^{-1}$) at 620 nm. The surface area is calculated by assuming that the beads are perfectly spherical and using the diameter given by the manufacturer. Roughness is neglected. The equation and correlation coefficient associated with the linear regression curve are computed with the mass concentration in mg·L$^{-1}$. The inset shows the DCVJ fluorescence spectra associated with the blank and the two outermost points of the main figure (see Figure S7 for the spectra arising from the other LB1 concentrations and Table S2 test 15 for the description of the setup).
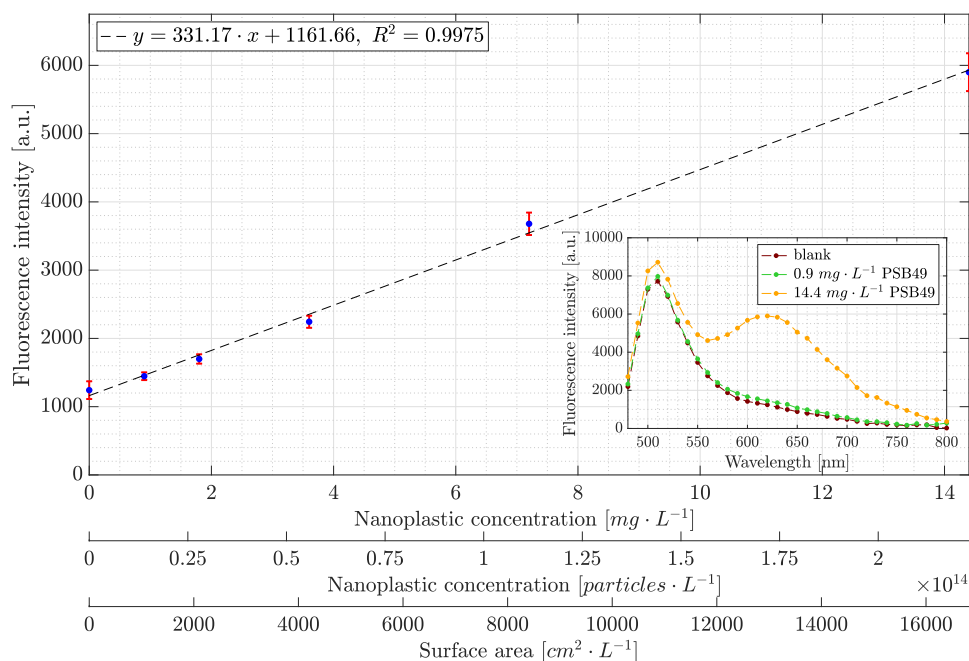


**Figure 2.** DCVJ fluorescence intensity as a function of the PSB49 concentration in terms of mass (0, 0.9, 1.8, 3.6, 7.2, and 14.4 mg·L$^{-1}$), number of particles (0, 1.39 × 10$^{13}$, 2.78 × 10$^{13}$, 5.57 × 10$^{13}$, 1.11 × 10$^{14}$, and 2.23 × 10$^{14}$ particles·L$^{-1}$), and surface area (0, 1050, 2099, 4198, 8397, and 16,793 cm$^2$·L$^{-1}$) at 620 nm. The surface area is calculated by assuming that the beads are perfectly spherical and using the diameter given by the manufacturer. Roughness is neglected. The equation and correlation coefficient associated with the linear regression curve are computed with the mass concentration in mg·L$^{-1}$. The inset shows the DCVJ fluorescence spectra associated with the blank and the two outermost points of the main figure (see Figure S9 for the spectra arising from the other PSB49 concentrations and Table S2 test 20 for the description of the setup).

on the fluorescence spectrum; hence, the corresponding calibration cannot be exploited (Figure S8). Associated with the emission peak and the steeper calibration slope, 620 nm was chosen as the suitable wavelength for PSN quantification.

The results of this calibration are displayed in Figure 1 as a triple x-axis plot representing the signal intensity as a function of the concentration in terms of mass, number of particles, and particle surface area.

Using the same mass concentrations, the data associated with the different PSB49 concentrations are even more distinguishable and the slope of the calibration seems steeper (Figure S9). However, the limit of quantification (LOQ) was not improved going from 100 to 49 nm PSNs. The resulting calibration is displayed in a triple *x*-axis plot (Figure 2).

PSN concentrations of 0, 0.9, 1.8, 3.6, 7.2, and 14.4 mg·L$^{-1}$ and the 620 nm DCVJ fluorescence peak were chosen for the next tests and calibrations.

**Influence of the Temperature and the Viscosity.** *Temperature Dependence.* A unique sequence of quadruplicates with increasing PSN concentration was analyzed at different temperatures, namely, 27−37 °C, in a cyclic way with 1 °C increments between each run. The results seem not to be distinguishable, and more replicates are needed to determine if there is a statistical significance (Tables S3 and S4 and Figure S10). In conclusion, further tests have to be conducted to unravel whether there is a real link between the temperature and the steepness of the slope of the calibration. In addition, whether successive irradiation of one sample has an effect on the result should also be investigated.

*Theoretical Viscosities.* Using the relation derived by Einstein to compute the viscosity $\eta$ of a nanofluid—a suspension of nanoparticles in a base fluid—and the Vogel−Fulcher−Tammann equation (see the Supporting Information, Section S2.6 for details) to obtain $\eta_{\text{base fluid}}$, it was demonstrated that the difference of viscosity between the blank and the most concentrated PSN standard (14.4 mg·L$^{-1}$) is negligible compared to the decrease in water viscosity when the temperature is increased by 1 °C.[39−41] In fact, a PSN suspension is a colloidal solution made of two distinct phases. It is not a fluid with a defined viscosity. Even if PSN suspensions could be identified as a nanofluid whose viscosity is described by Einstein, the results presented in Table S5 suggest that the DCVJ fluorescence is not affected by a viscosity change but rather by hydrophobic interactions with the plastic beads.

*Influence of the Addition of Glycerol to PSN.* Since DCVJ's fluorescence is affected by its microenvironment and especially the viscosity of the media, it is important to study whether PSNs are still quantifiable in such media. In the presence of glycerol, the 510 nm emission peak of DCVJ increases linearly with the concentration of the viscous fluid (Figures S11−S13). PSN quantification becomes more challenging when the concentration of glycerol is increased. The viscous media induce an upward shift of the emission spectra, the 620 nm fluorescence peak disappears with increasing glycerol percentage, and the slope of the calibration decreases (Table S7). When mixed with a viscous compound, the DCVJ fluorescence spectrum varies at a different wavelength compared to the presence of increasing PSN concentration (510 nm versus 620 nm). It suggests that each peak is associated with a distinct interaction or phenomenon. Thus, it confirms that the detection of PSN is not due to an increase in viscosity but rather to a hydrophobic interaction, which is increasingly pronounced with the particle's concentration, between the fluorescent rotor and the hydrophobic surface of the nanoparticles.

**Influence of the PSN Characteristics.** *Surface Area vs Diameter.* At an equal surface area, LB1 leads to the most intense emission signal at 620 nm followed by PSB49 and finally LB3 (Figure S14). Interestingly, the order does not follow the size of the beads as before when the analyses were

done at equal mass concentration. The higher the surface area, the more interactions with DCVJ, and the more intense the signal becomes. Although the surface area has the most influence on the fluorescence, the particle size also plays a role. It should also be kept in mind that PSB49 and LB1/LB3 are produced by two distinct manufacturers. This probably has an impact on the results if the shape and the roughness of the beads are not exactly the same.

*Influence of Nanoplastic Functionalization.* Carboxyl-functionalized PSNs can be found in the environment due to aging of pristine beads or to an intended functionalization to confer special properties. At equal mass concentration, the fluorescence intensity of DCVJ at 620 nm is higher in the presence of PSB49 than in PSB49coo. Since DCVJ is hydrophobic, it has more affinity for PSB49 than for PSB49coo and it is translated by a lower fluorescence signal at 620 nm. Although the trend illustrated in Figure S15 can be explained by that theory and even if the slope of the calibration is higher with PSB49 (368 ± 5) than with PSB49coo (338 ± 14), statistical tests over the quadruplicates at 620 nm reveal that the results are significantly different only for the 7.2 mg·L$^{-1}$ data points (*t* test, *p* = 0.0044). However, the degree of functionalization is not known. More replicates are needed to confirm the results, and further experiments with even more hydrophilic or hydrophobic functionalized PS beads should be conducted to study deeper the influence of the chemical surface. The pH of the samples and its effect have also to be further investigated. It could shed light on the interaction between DCVJ and the NPs since the pH modulates the hydrophobicity of the surface of the functionalized beads, according to the pKa of the functional groups. It is also worth mentioning that this experiment indicates that the DCVJ methodology could be applied with other types of NPs. To our knowledge, the only commercially available NPs, i.e., standardized and usable for analytical method development, are the polystyrene ones.

**PSN Quantification in Water and Influence of the Natural Organic Matter.** *Linearity and LOD/LOQ.* Exploring the lower and higher limit of exploitable LB1 and PSB49 concentrations, it was shown that, between 0 and 0.8 mg·L$^{-1}$, it is not possible to quantify those PSNs and the relationship between the fluorescence signal and PSN concentration is no longer linear when the concentrations are increased to 28.8 and 57.6 mg·L$^{-1}$ (Figure S16). In addition to being visually observed, it can be assessed by the decrease in the correlation coefficient ($R^2$) going from 0−14.4 mg·L$^{-1}$ ($R^2$ = 0.9997) to 0−28.8 mg·L$^{-1}$ ($R^2$ = 0.9826) and finally the 0−57.6 mg·L$^{-1}$ ($R^2$ = 0.8621) linear regression for LB1. With PSB49 at concentrations higher than 14.4 mg·L$^{-1}$, the loss of linearity is less pronounced than with LB1 but it is still noticeable (test 25; Table S2 and Figure S16). It can be assessed by the decrease in the $R^2$ value from 0−14.4 mg·L$^{-1}$ ($R^2$ = 0.9971) to 0−28.8 mg·L$^{-1}$ ($R^2$ = 0.9945) and finally the 0−57.6 mg·L$^{-1}$ ($R^2$ = 0.9504) linear regression. Restricting the calculations to the data from the tests performed in pure water with the final method settings and PSN concentrations (0, 0.9, 1.8, 3.6, 7.2, and 14.4 mg·L$^{-1}$) as well as a temperature between 25 and 26 °C, the PSN limits of detection (LODs) were found to be 518 $\mu$g·L$^{-1}$ (9.42 × 10$^{11}$ particles·L$^{-1}$) for LB1 and 475−563 $\mu$g·L$^{-1}$ (7.34 × 10$^{12}$ to 8.7 × 10$^{12}$ particles·L$^{-1}$). The corresponding LOQ amounts to 1.725 mg·L$^{-1}$ (3.14 × 10$^{12}$ particles·L$^{-1}$) for LB1 and ranges from 1.582 to 1.875 mg·L$^{-1}$ (2.43 × 10$^{13}$ to 2.90 × 10$^{13}$ particles·L$^{-1}$) for PSB49. In the

absence of data regarding the concentration and distribution of NPs in the environment, our results could only be compared to the prediction given in the literature.[42] The obtained LOD and LOQ values are higher than the modelized range of 1 ng·L$^{-1}$ to 1 $\mu$g·L$^{-1}$ for the particle sizes used in the present work. However, they match the concentrations commonly used in NP ecotoxicological studies. As the ultimate goal is to use the method with environmental samples, it would be of interest to measure the pH in the field and determine if a pH optimization is required to still be able to detect and quantify nanoplastics in environmental samples.

*Influence of the NOM.* As a step toward more environmentally realistic conditions, the NOM was used to assess the efficiency of the method when PSNs are found in environmental water. At 1.6 mg·L$^{-1}$ (an environmentally realistic concentration), the fluorescence of the NOM in the 610–640 nm region is very low compared to the signal of DCVJ (Figure S17). Therefore, the fluorescence of the NOM does not interfere with the DCVJ one (slope of the calibration $m_{PSB49, \, NOM}$ = 340 ± 6 and $m_{LB1, \, NOM}$ = 254 ± 5 in the presence of the NOM compared to $m_{PSB49, \, pure \, water}$ = 331 ± 8 and $m_{LB1, \, pure \, water}$ = 317 ± 11 in its absence). These experiments show that, even in the presence of the organic matter from the Mississippi River, the developed PSN detection method can be used for 50 and 100 nm diameter PSNs (Figure S18).

**PSN Quantification in Biological Samples.** *Analysis of PSN in Vegetal Samples.* The stem of the dried radish sprouts was difficult to crush finely. Due to the additional cell wall mainly made of cellulose, the vegetal material requires harsher conditions for them to be digested than animal tissues. Two possibilities were considered. The remaining pieces of radish sprouts could be either digested using hydrogen peroxide (H$_2$O$_2$) or filtered. The potential loss of the vegetal matter in the filter during the sample preparation was chosen over the risk of an alteration of PSNs and DCVJ due to H$_2$O$_2$ oxidative properties. Even if the dry radish sprout concentration after filtration (0.45 $\mu$m PTFE) is not exactly known, a comparison between the experiments with increasing concentration of vegetal tissues is still possible.

*Matrix Effect and LOD/LOQ.* The radish matrix fluorescence does not interfere with the DCVJ 620 nm emission peak (test RA-1; Table S10 and Figure S19). At that location, the radish sprout signal even reaches its minimum intensity. Adding PSB49 and DCVJ in the radish sprout matrix (tests RA-2 to RA-5), the characteristic 620 nm peak arising from the presence of PSNs is broader than for a pure water matrix. By increasing the concentration of radish sprouts, the 680 nm matrix peak grows until exceeding the 620 nm peak height and forming a defined peak (Figures S20–S23). Although the matrix concentration is similar, its associated emission at 680 nm seems to increase with the concentration of PSB49. Given the absorbance spectra of carotenoids and chlorophyll, the emissive species present in leaves may be excited by the DCVJ's fluorescence.[43–45] The slope of the linear regression at 620 nm decreases with the increase in radish sprout concentration (Table S11). The calibration, obtained with the standards (spiked with PSB49 after the matrix filtration), was used to compute the concentration of the samples (spiked before filtration) and their recovery rate to assess the developed analytical method in the presence of a vegetal matrix. At the two lowest radish matrix concentrations (RA-2 and RA-3), the recovery rate varies relatively little. The less

than 100% recovery may be due to the trapping of PSB49 in the undissolved vegetal tissues. These are mainly constituted of cellulose, the most difficult part of the matrix to dissolve, and the adsorption of 55 nm diameter PSNs (virgin and carboxylate functionalized) on cellulose films mimicking vegetal tissues has already been demonstrated.[46] Curiously, the increase in the radish sprout content does not lead to a decrease in the PSN recovery rate as it could have been expected by the abovementioned trapping hypothesis. DCVJ seems to detect more beads than there are. Since the detection of PSNs is based on their hydrophobic interaction with DCVJ, the rotor may interact with another hydrophobic substance. The possibility of an inflow of particles from the filter should be investigated. The idea would be to avoid the filtration step. To do so, a procedure must be found to crush the radish sprouts in a completely soluble (i.e., extremely fine) powder. It could also be possible that the calibration slopes from RA-4 and RA-5 are underestimated due to an issue during the measurement and lead to higher recovery rate calculations. Alternatively, the matrix effect may be too strong around 128 mg·L$^{-1}$ dry radish sprouts. More tests should be conducted to determine whether a radish concentration limit, beyond which PSNs cannot be reliably quantified, exists. It is worth mentioning that the standards were measured in the same matrix as the samples to account for a possible filtering effect. That is also the case for the experiments with mussels.

*Analysis of PSN in Animal Samples.* Mussels were chosen for the application of the method in animal tissues because, being filter feeders, they are particularly exposed to NP ingestion.[47] They ingest phyto- and zooplankton by filtering water. Like their feed, NPs are found in suspension and are then prone to contaminate mussels by erroneous intake.[48–50] In addition, mussels are widely available and offer the possibility to compare results with the literature.[32] During test MU-1, the D1 mix was not useful to homogenize the mussel paste. The Sdiluted16% supernatant was relatively opaque, and its fluorescence signal was consequently pronounced even in the absence of DCVJ (Figure S25). Thanks to the freeze-drying process followed by pestle crushing used for the other tests, a finer and more homogeneous material was obtained. In addition, since water is completely removed, the weighed mass of mussels stomach powder (MSP) can reliably be reproduced. Otherwise, the water content is challenging to assess when the animal tissues are cooked and shredded without any additional step.

*Matrix Effect and LOD/LOQ.* By increasing the mussel tissue content (going from a filtered to nonfiltered matrix, tests MU-2 and MU-3), a peak in the 670–680 nm region appears and grows with the concentration of PSB49 (Figures S26 and S27). According to the linear regression plots, the mussel matrix does not impede the calibration. With the filtered matrix, the slope at 620 nm, 381 ± 10, was the highest one over the spectrum (Figure S26). This is not the case with the nonfiltered matrix, giving rise to its steeper slope at 670 nm (394 ± 27), whereas $m$ = 323 ± 5 at 620 nm (Figure S27). However, as displayed in Figure S26 and judged by the correlation coefficient ($R^2$ = 0.9813 at 670 nm compared to 0.9991 at 620 nm), the calibration is more reliable at 620 nm. The increase in the matrix 670 nm peak could be due to an energy transfer between DCVJ and the phaeopigment, which emits around 670 nm.[51] However, given the complexity of the mussel matrix, which depends on its diet, it is not possible to be more accurate at that point.

The MSP matrix concentration in the microplate wells was increased to $\approx 4$ g·L$^{-1}$ for the next tests (MU-4 to MU-7). It is important to assess the performance of the NP detection-developed method in the presence of such higher biological material concentration since the concentration of NPs in a single organism is expected to be relatively low; hence, a large amount of material is needed to reach the LOD.[42] The high MSP concentration explains the addition of a digestion step. As a water bath was now used, the mix D1 (from the literature[32]) was tested again. Alternatively, KOH 10%, reported to be the most promising digestion procedure without NP alteration,[52] was also used. Visually, the dissolution of MSP was improved by the additional digestion step. After centrifugation, a light orange transparent solution above a tiny amount of undissolved dark material was obtained from test MU-5 (KOH digestion). The volume of the remaining mussel tissues was greater in the tubes associated with MU-4 (mix D1 digestion), and the supernatant was greenish and rather cloudy. Unfortunately, neither digestive conditions allowed us to differentiate the blank and the samples mimicking environmental conditions. Including the standard deviation over the quadruplicates, the data are not significantly different (Figure S28). Unsurprisingly, the mix D1 and H$_2$O give rise to the same spectrum (Figure S29, blue curve hidden under the violet one). This is also the case in the presence of DCVJ (orange and yellow curves). The 680 nm peak of the MSP supernatant digested with the mix D1 is almost three times less intense than when mixed with DCVJ (light brown and maroon curves).

Interestingly, the same cannot be said about the fluorescence spectra recorded from test MU-5. The spectra corresponding to water and KOH mixed with either water or DCVJ appear to be stacked on top of each other (blue, violet, and yellow curves of Figure S30), and the spectrum of the supernatant of MSP digested with KOH (light brown curve) seems to peak higher than the blank and the samples. This suggests that DCVJ reacts with KOH, and DCVJ fluorescence is quenched. Thus, in the experiment with KOH, the matrix fluorescence is more intense when it is simply diluted in water than when it is mixed with DCVJ. Based on visual and spectral analysis, KOH is a better digestive media than the mix D1. After digestion and centrifugation, the 680 nm emission of the mussel matrix treated with KOH is more than 3.5 higher than when the mix D1 was used (Figures S29 and S30, brown curve).

The standards analyzed in an $\approx 4$ g·L$^{-1}$ MSP matrix (tests MU-6 and MU-7) lead to emission curves close to each other at any wavelength (Figures S31−S34). The usual peak increase at 620 nm with the PSB49 concentration is not visible. The 620 nm signal of the DCVJ probe is buried under the fluorescence emission of the matrix (680 nm), limiting the maximal acceptable concentration of the matrix to $\approx 16$ mg·L$^{-1}$ in the PSN assays. As already noticed, DCVJ fluorescence is again suppressed in the presence of KOH, and given its high fluorescence intensity, the matrix is better digested (Figure S32, light gray and light brown curves). Additional tests should be conducted to unravel why PSNs could not be quantified. PSB49 should remain in suspension even after 15 min of centrifugation at 3000 rpm and not be degraded by KOH basic conditions.[22,32,52] However, trapping by the biological tissues could happen and drag the plastic particles at the bottom of the tube, removing them from the supernatant.

## CONCLUSIONS

An innovative analytical method for detecting and quantifying PSNs by means of a fluorescent molecular rotor emission was further developed. The three-unit molecular system was already extensively studied for viscosity probing. However, only two recent studies exploit DCVJ, a commercially available FMR, to determine the concentration of nanosized plastic beads. The underlying phenomenon was confirmed to be a hydrophobic interaction between the probe and the analyte rather than the viscosity resulting from the presence of the nanomaterial, which was found to be negligible. Starting with the procedure given in previous works, different factors influencing the signal were tested in a systematic way. The most important parameters were found to be the choice of the solvent to prepare the fluorescent probe stock solution and the volume ratio of the analyte to DCVJ solutions. The PSN standard concentration must also be carefully chosen to be above the LOQ and below the limit where linearity is lost. By studying the modulation of the emission spectrum of DCVJ mixed with increasing concentrations of PSNs, the appearance and increase in a second band at 620 nm due to hydrophobic interactions with the beads were found to be the most suitable to detect and quantify the PSNs in aqueous media. Given the nature of the interaction between DCVJ and the PSNs, the surface area has the most influence on the fluorescence. However, the particle size also plays a role.

While PSB49 was quantifiable at concentrations typically used in ecotoxicological studies in all studied matrices, LB1 results were less distinct. Although the size of LB3 seems to be a limiting factor for its quantification by the developed analytical method, other techniques—currently under development—would be more suitable.

Increasing the complexity of the matrix from pure water to aqueous solution of natural organic matter, the method was still efficient. However, the next step toward environmental samples was more challenging to achieve and an additional digestion step was required. While quantification of PSNs in dry radish sprouts and mussels spiked with PSB49 was promising at matrix concentrations ranging from 20 to 200 mg·L$^{-1}$, the sample preparation should be improved to overcome the issues encountered at a higher non-analyte content. To further optimize the method, the interactions between DCVJ, the plastics, and the compounds constituting the environmental matrix as well as its pH have to be studied in greater depth. In addition, it would be interesting to measure the PSN suspensions with another method, such as Py-GC−MS, and compare the results.

The developed method presents the advantages of being label-free and easy to implement in terms of equipment and handling. It would thus be worth investigating further this NP detection technique to reach standardization for routine analysis. To conclude, our work presents the feasibility to quantify PSNs by exploiting DCVJ fluorescence and the remaining points to explore. Being one of the first works on that subject, it opens the door to new perspectives in the challenging NP field.

## ASSOCIATED CONTENT

### ⓢ Supporting Information

The Supporting Information is available free of charge at https://pubs.acs.org/doi/10.1021/acs.analchem.1c02055.

Section S1: "Materials and preliminary measurements" with sample handling; preliminary measurements, Section S2: "Method development" with microplate reader settings (Table S1); measurement procedure; DCVJ's fluorescence analysis (Figures S3–S5); tests realized to investigate and improve DCVJ's response to PSNs (Table S2 and Figures S6–S9); assessment of the influence of different factors (Tables S3–S9 and Figures S9–S17), and Section S3: "Method application" with radish sprout and mussel sample preparation (Figure S23); tests of PSN detection and quantification in biological tissues (Tables S10 and S11 and Figures S18–22 for radish sprouts; Table S12 and Figures S24–S34 for mussels) (PDF)

## ■ AUTHOR INFORMATION

### Corresponding Author

**Florian Breider** − *Ecole Polytechnique Fédérale de Lausanne − EPFL, Central Environmental Laboratory, ENAC, IIE, Station 2, Lausanne CH-1015, Switzerland;* ⓘ orcid.org/0000-0002-5698-0314; Email: florian.breider@epfl.ch

### Author

**Angélique Moraz** − *Ecole Polytechnique Fédérale de Lausanne − EPFL, Central Environmental Laboratory, ENAC, IIE, Station 2, Lausanne CH-1015, Switzerland*

Complete contact information is available at:
https://pubs.acs.org/10.1021/acs.analchem.1c02055

### Notes

The authors declare no competing financial interest.

## ■ REFERENCES

(1) *Global plastic production 1950−2019.* https://www.statista.com/statistics/282732/global-production-of-plastics-since-1950/ (accessed 2021−05 -14).

(2) Carpenter, E. J.; Smith, K. L., Jr. *Science* **1972**, *175*, 1240−1241.

(3) Liu, Z.; Liu, W.; Walker, T. R.; Adams, M.; Zhao, J. *J. Environ. Manage.* **2021**, *287*, 112283.

(4) Ryberg, M. W.; Hauschild, M. Z.; Wang, F.; Averous-Monnery, S.; Laurent, A. *Resour., Conserv. Recycl.* **2019**, *151*, 104459.

(5) Guerranti, C.; Martellini, T.; Perra, G.; Scopetani, C.; Cincinelli, A. *Environ. Toxicol. Pharmacol.* **2019**, *68*, 75−79.

(6) De Falco, F.; Gullo, M. P.; Gentile, G.; Di Pace, E.; Cocca, M.; Gelabert, L.; Brouta-Agnésa, M.; Rovira, A.; Escudero, R.; Villalba, R.; Mossotti, R.; Montarsolo, A.; Gavignano, S.; Tonin, C.; Avella, M. *Environ. Pollut.* **2018**, *236*, 916−925.

(7) Hartmann, N. B.; Rist, S.; Bodin, J.; Jensen, L. H.; Schmidt, S. N.; Mayer, P.; Meibom, A.; Baun, A. *Integr. Environ. Assess. Manage.* **2017**, *13*, 488−493.

(8) Boucher, J.; Faure, F.; Pompini, O.; Plummer, Z.; Wieser, O.; Felippe de Alencastro, L. *TrAC, Trends Anal. Chem.* **2019**, *112*, 66−74.

(9) Jeyasanta, K. I.; Sathish, N.; Patterson, J.; Edward, J. K. P. *Mar. Pollut. Bull.* **2020**, *154*, 111055.

(10) Gigault, J.; ter Halle, A.; Baudrimont, M.; Pascal, P.-Y.; Gauffre, F.; Phi, T.-L.; El Hadri, H.; Grassl, B.; Reynaud, S. *Environ. Pollut.* **2018**, *235*, 1030−1034.

(11) Hernandez, L. M.; Yousefi, N.; Tufenkji, N. *Environ. Sci. Technol. Lett.* **2017**, *4*, 280−285.

(12) Auta, H. S.; Emenike, C. U.; Fauziah, S. H. *Environ. Int.* **2017**, *102*, 165−176.

(13) Xu, M.; Halimu, G.; Zhang, Q.; Song, Y.; Fu, X.; Li, Y.; Li, Y.; Zhang, H. *Sci. Total Environ.* **2019**, *694*, 133794.

(14) Forte, M.; Iachetta, G.; Tussellino, M.; Carotenuto, R.; Prisco, M.; De Falco, M.; Laforgia, V.; Valiante, S. *Toxicol. In Vitro* **2016**, *31*, 126−136.

(15) de Souza Machado, A. A.; Kloas, W.; Zarfl, C.; Hempel, S.; Rillig, M. C. *Global Change Biol.* **2018**, *24*, 1405−1416.

(16) Amereh, F.; Babaei, M.; Eslami, A.; Fazelipour, S.; Rafiee, M. *Environ. Pollut.* **2020**, *261*, 114158.

(17) Liu, Z.; Yu, P.; Cai, M.; Wu, D.; Zhang, M.; Huang, Y.; Zhao, Y. *Chemosphere* **2019**, *215*, 74−81.

(18) Zhang, W.; Liu, Z.; Tang, S.; Li, D.; Jiang, Q.; Zhang, T. *Chemosphere* **2020**, *238*, 124563.

(19) Yuan, W.; Zhou, Y.; Liu, X.; Wang, J. *Environ. Sci. Technol.* **2019**, *53*, 12715−12724.

(20) Barbosa, F.; Adeyemi, J. A.; Bocato, M. Z.; Comas, A.; Campiglia, A. *Environ. Res.* **2020**, *182*, 109089.

(21) Wang, L.; Wu, W.-M.; Bolan, N. S.; Tsang, D. C. W.; Li, Y.; Qin, M.; Hou, D. *J. Hazard. Mater.* **2021**, *401*, 123415.

(22) Schwaferts, C.; Niessner, R.; Elsner, M.; Ivleva, N. P. *TrAC, Trends Anal. Chem.* **2019**, *112*, 52−65.

(23) Mintenig, S. M.; Bäuerlein, P. S.; Koelmans, A. A.; Dekker, S. C.; Van Wezel, A. P. *Environ. Sci.: Nano* **2018**, *5*, 1640−1649.

(24) Nguyen, B.; Claveau-Mallet, D.; Hernandez, L. M.; Xu, E. G.; Farner, J. M.; Tufenkji, N. *Acc. Chem. Res.* **2019**, *52*, 858−866.

(25) Bolea-Fernandez, E.; Rua-Ibarz, A.; Velimirovic, M.; Tirez, K.; Vanhaecke, F. *J. Anal. At. Spectrom.* **2020**, *35*, 455−460.

(26) Jiménez-Lamana, J.; Marigliano, L.; Allouche, J.; Grassl, B.; Szpunar, J.; Reynaud, S. *Anal. Chem.* **2020**, *92*, 11664−11672.

(27) Frehland, S.; Kaegi, R.; Hufenus, R.; Mitrano, D. M. *Water Res.* **2020**, *182*, 115860.

(28) Bhagat, J.; Zang, L.; Nishimura, N.; Shimada, Y. *Sci. Total Environ.* **2020**, *728*, 138707.

(29) Jiang, X.; Tian, L.; Ma, Y.; Ji, R. *Sci. Total Environ.* **2019**, *655*, 591−597.

(30) Al-Sid-Cheikh, M.; Rowland, S. J.; Stevenson, K.; Rouleau, C.; Henry, T. B.; Thompson, R. C. *Environ. Sci. Technol.* **2018**, *52*, 14480−14486.

(31) Bisso, P. W.; Tai, M.; Katepalli, H.; Bertrand, N.; Blankschtein, D.; Langer, R. *Nano Lett.* **2018**, *18*, 618−628.

(32) Gagné, F. *J Xenobiot.* **2019**, DOI: 10.4081/xeno.2019.8147.

(33) Haidekker, M. A.; Theodorakis, E. A. *J. Biol. Eng.* **2010**, *4*, 11.

(34) Loutfy, R. O.; Arnold, B. A. *J. Phys. Chem.* **1982**, *86*, 4205−4211.

(35) Haidekker, M. A.; Ling, T.; Anglo, M.; Stevens, H. Y.; Frangos, J. A.; Theodorakis, E. A. *Chem. Biol.* **2001**, *8*, 123−131.

(36) Kuimova, M. K. *Phys. Chem. Chem. Phys.* **2012**, *14*, 12671−12686.

(37) Saunders, F. L. *J. Colloid Sci.* **1961**, *16*, 13−22.

(38) Gavvala, K.; Sasikala, W. D.; Sengupta, A.; Dalvi, S. A.; Mukherjee, A.; Hazra, P. *Phys. Chem. Chem. Phys.* **2013**, *15*, 330−340.

(39) Einstein, A. *Ann. Phys.* **1906**, *324*, 289−306.

(40) Udawattha, D. S.; Narayana, M.; Wijayarathne, U. P. L. *J. King Saud Univ.,-Sci.* **2019**, *31*, 412−426.

(41) Viswanath, D. S.; Ghosh, T.; Prasad, D. H. L.; Dutt, N. V. K.; Rani, K. Y. *Viscosity of Liquids: Theory, Estimation, Experiment, and Data*; Springer Netherlands: 2007; DOI: 10.1007/978-1-4020-5482-2.

(42) Lenz, R.; Enders, K.; Nielsen, T. G. *Proc. Natl. Acad. Sci.* **2016**, *113*, E4121−E4122.

(43) Buschmann, C.; Langsdorf, G.; Lichtenthaler, H. K. *Photosynthetica* **2000**, *38*, 483−491.

(44) Zang, L.-Y.; Sommerburg, O.; van Kuijk, F. J. G. M. *Free Radical Biol. Med.* **1997**, *23*, 1086−1089.

(45) Kleinegris, D. M. M.; van Es, M. A.; Janssen, M.; Brandenburg, W. A.; Wijffels, R. H. *J. Appl. Phycol.* **2010**, *22*, 645−649.

(46) Bhattacharya, P.; Chen, R.; Lard, M.; Lin, S.; Ke, P.-C. Binding of Nanoplastics onto a Cellulose Film. In *2010 3rd International Nanoelectronics Conference (INEC)*; 2010; pp. 803−804, DOI: 10.1109/INEC.2010.5425197.

(47) Collard, F.; Gasperi, J.; Gilbert, B.; Eppe, G.; Azimi, S.; Rocher, V.; Tassin, B. *Sci. Total Environ.* **2018**, *643*, 1257−1264.

(48) Wegner, A.; Besseling, E.; Foekema, E. M.; Kamermans, P.; Koelmans, A. A. *Environ. Toxicol. Chem.* **2012**, *31*, 2490−2497.

(49) Cho, Y.; Shim, W. J.; Jang, M.; Han, G. M.; Hong, S. H. *Environ. Pollut.* **2019**, *245*, 1107−1116.

(50) Li, L.-L.; Amara, R.; Souissi, S.; Dehaut, A.; Duflos, G.; Monchy, S. *Sci. Total Environ.* **2020**, *745*, 141018.

(51) Gelder, S. R.; Robinson, W. E. *J. Exp. Mar. Biol. Ecol.* **1980**, *43*, 281−292.

(52) Dehaut, A.; Cassone, A.-L.; Frère, L.; Hermabessiere, L.; Himber, C.; Rinnert, E.; Rivière, G.; Lambert, C.; Soudant, P.; Huvet, A.; Duflos, G.; Paul-Pont, I. *Environ. Pollut.* **2016**, *215*, 223−233.